Science of Sintering, **53** (2021) 237-252

https://doi.org/10.2298/SOS2102237R

UDK: 661.847; 612.086.3; 796.911.5:178; 532.74

TEM and DFT Study of Basal-plane Inversion Boundaries in SnO_2-doped ZnO

Vesna Ribić[1*)], Aleksander Rečnik[2], Goran Dražić[3], Matejka Podlogar[2], Zorica Branković[1], Goran Branković[1]

[1]Department of Materials Science, Institute for Multidisciplinary Research, University of Belgrade, Kneza Višeslava 1, Belgrade, Serbia

[2]Department for Nanostructured Materials, Jožef Stefan Institute, Jamova cesta 39, Ljubljana, Slovenia

[3]Department of Materials Chemistry, National Institute of Chemistry, Hajdrihova 19, Ljubljana, Slovenia

Abstract:

In our recent study (Ribić et al. 2020) we reported the structure of inversion boundaries (IBs) in Sb_2O_3-doped ZnO. Here, we focus on IBs that form in SnO_2-doped ZnO. Using atomic resolution scanning transmission electron microscopy (STEM) methods we confirm that in SnO_2-doped ZnO the IBs form in head-to-head configuration, where ZnO_4 tetrahedra in both ZnO domains point towards the IB plane composed of a close-packed layer of octahedrally coordinated Sn and Zn atoms. The in-plane composition is driven by the local charge balance, following Pauling's principle of electroneutrality for ionic crystals, according to which the average oxidation state of cations is 3+. To satisfy this condition, the cation ratio in the IB-layer is Sn^{4+}: Zn^{2+}=1:1. This was confirmed by concentric electron probe analysis employing energy dispersive spectroscopy (EDS) showing that Sn atoms occupy 0.504 ± 0.039 of the IB layer, while the rest of the octahedral sites are occupied by Zn. IBs in SnO_2-doped ZnO occur in the lowest energy, IB_3 translation state with the cation sublattice expansion of $\Delta IB_{(Zn–Zn)}$ of +91 pm with corresponding O-sublattice contraction $\Delta IB_{(O–O)}$ of –46 pm. Based on quantitative HRTEM and HAADF–STEM analysis of in-plane ordering of Sn and Zn atoms, we identified two types of short-range distributions, (i) zigzag and (ii) stripe. Our density functional theory (DFT) calculations showed that the energy difference between the two arrangements is small (~6 meV) giving rise to their alternation within the octahedral IB layer. As a result, cation ordering intermittently changes its type and the direction to maximize intrinsic entropy of the IB layer driven by the in-plane electroneutrality and 6-fold symmetry restrictions. A long-range in-plane disorder, as shown by our work would enhance quantum well effect to phonon scattering, while Zn^{2+} located in the IB octahedral sites, would modify the bandgap, and enhance the in-plane conductivity and concentration of carriers.

Keywords*: Inversion domain boundary (IDB); Sn-doped ZnO; Polarity engineering; Thermoelectrics; Optoelectronics.*

1. Introduction

Nonohmic properties of ZnO ceramics with a complex metal-oxide additions attracted researchers already 50 years ago for its use in varistor applications [1]. Successive studies

*) **Corresponding author:** vesna.ribicka@gmail.com

were discovering new additives [2, 3] and processing methods [4] to improve varistor's properties. The first to investigate the role of Sn addition in ZnO varistor ceramics were Gould and Carter [5], who recorded power-law dependence of current density on applied voltage, which they interpreted in terms of space-charge-limited conduction controlled by an exponential distribution of traps. In nearly the same time, grain growth and electrical properties of complex ZnO-based varistor compositions with SnO_2 additions were investigated by Milošević *et al.* [6]. As SnO_2, as a dopant, did not significantly improve varistor properties, it had gone forgotten, until Daneu *et al.* [7] discovered the most unusual phenomenon, when studying grain growth in $ZnO–Bi_2O_3–SnO_2$ ceramics. On small additions of SnO_2 the ZnO grains grew significantly larger than without its addition. This alone would not be alarming, if then with higher additions of SnO_2 the ZnO grain size would not decrease. What was happening? How the low additions of a dopant first enhance the grain growth of the main phase, while increasing addition of the same dopant then inhibits its growth. The authors found that every ZnO grain in the final microstructure contains an inversion boundary (IB). Each grain with such IB grows on the expense of 'normal' ZnO grains until they dominate the microstructure. With higher amount of added SnO_2, more IBs form in the initial ZnO grains, and final grain sizes are smaller. This behavior was called 'IB-induced grain growth' and was shown to be the key mechanism to tune grain growth in ZnO ceramics from a fine- to coarse-grained by a strict control of IBs [8-13]. Meanwhile, other researchers were exploring varistor properties of mixed ZnO/SnO_2 ceramics [14].

IBs in ZnO have soon been studied by electron microscopy methods. In structural and spectroscopic investigation of Sb-rich IBs, Rečnik *et al.* [15] reported that IBs in ZnO are always triggered by specific IB-forming dopant and that they compose an octahedral IB layer of cations with an average oxidation state of 3+. For Sn, being in the oxidation state of 4+, they suggested that it would constitute an octahedral IB layer together with Zn^{2+} in the ratio of 1:1. For the first time implementing the new method for quantitative chemical analysis of interfaces [16], Daneu *et al.* accurately measured the composition of Sn-rich IB and proposed the model of its local structure [17]. With spectroscopic and structural analysis of IBs in SnO_2-doped ZnO it was unequivocally shown that, controlled by the charge balance rule [15], Sn constitutes exactly one half of the IB layer.

Besides in varistor ceramics, Sn-doping is widespread also in ZnO thin films, synthesis of nanobelts, nanowires and other less common nanostructures, however its mode of incorporation in ZnO is generally unclear. Sn is known as paramount n-type dopant for ZnO thin films [18]. It increases the porosity and surface area of ZnO films [19,20] giving Sn-doped ZnO films excellent sensing characteristics [21-24]. Doping with SnO_2 improves optical properties [25-29], modifies ZnO band gap [30-32], enhances the transmittance from visible light to near-IR range [33-36], enhances electrical conductivity [37,38] and the transport properties through lower resistivity and higher donor concentration [39]. Sn-doped ZnO films found diverse applications in dye sensitized solar cells [40-43], photocatalysis [44-46], piezoelectric devices [47] and even thermoelectrics [48]. Many of these studies noticed larger grain size with low additions of SnO_2 and smaller grain size with higher additions [19, 35, 40, 49, 50]. This grain growth behavior is quite interesting, and suggests that they also may have IBs, and the grain growth adheres to the IB-induced grain growth mechanism, as suggested by Daneu *et al.* in SnO_2-doped ZnO ceramics [7], moreover so, as Sn^{4+} is known to have no solid solution with ZnO, and it forms Sn-rich IBs as soon as it enters the ZnO structure [10].

In polycrystalline thin films IBs are not easy to detect, and their preparation would necessitate a plan-view TEM sample preparation [51]. More readily, IBs are observed in diverse nanostructures. Deng *et al.* [52] noticed IBs in Sn-doped ZnO nanobelts, extending along the longer $[01\bar{1}0]$ axis of the belts, beautifully demonstrating the IB-induced anisotropic growth mechanism [10]. Similar conclusions were made by other authors [53, 54]. Observation of IBs in Sn-doped ZnO nanobelts and nanowires was followed by highly

competitive studies of their atomic structure using scanning transmission electron microscopy (STEM) methods [55-59]. While most of these studies correctly interpret the translation state of Sn-rich IBs, their lack in understanding of the local charge balance [15] is reflected in erroneous interpretation of the occupancy and arrangement of Sn atoms in the IB-plane. While it is generally known that Sn alone cannot produce a stable tail-to-tail inversion [10] further deficiency in these studies is seen in their knowledge on stabilization of parallel Sn-rich IBs. Not being aware of contamination with Ga [55], In [57], Si [58] or Al [59] in their experiments, they report on growing pure polytypoidic $SnO_2(ZnO:Sn)_m$ nanowires, instead of fully characterizing these fascinating mixed homologous phases with potentially interesting physical properties. Namely, in addition to Fe and Ti, these dopants are known to stabilize tail-to-tail configuration of IBs [60-65], enabling growth of mixed homologous structures with Sn-rich IBs, as this was clearly demonstrated by Eichhorn *et al.* [60] and Hoemke *et al.* [63] for gallium and aluminum additions.

While regardless of their synthesis route, the literature data has a broad agreement on the translation state of Sn-rich IBs in ZnO and octahedral coordination of Sn, there are still ambiguities about the occupancy, and thus no consent about the arrangement Sn atoms in the IB-layer. In the present study we investigated the structure and chemistry of basal-plane IBs in SnO_2-doped ZnO ceramics by means of high-resolution transmission electron microscopy (HRTEM), high-angle annular dark-filed (HAADF) and annular bright filed (ABF) STEM methods to study the local structure, and energy dispersive X-ray spectroscopy (EDS) to determine the chemical composition of Sn-rich IBs in ZnO. Experimental studies are complemented by structure modeling and density functional theory (DFT) calculations to identify the lowest energy cation distributions in the IB-layer.

2. Materials and Experimental Procedures

2.1 Sample preparation

The pellets of ZnO with Bi_2O_3 and SnO_2 additions were prepared by mixing the oxide powders and sintered at 1200 °C for 2 hours. Here, SnO_2 addition acts as grain growth modifier [12] whereas Bi_2O_3 is added as fast oxygen ion conductor [66] increasing grain boundary resistivity in varistor compositions. Details of sample processing are given in ref. [7]. The pellets were cut and polished, and cross-sections were etched in diluted HCl to reveal ceramic microstructure with IBs. Prior to observations the samples were sputtered by a thin layer of carbon to improve conductivity. TEM samples were prepared according to the standard sample preparation procedure by ultrasonic cutting ceramic pellets into 3 mm disks (Sonicut 380, SBT Ltd., California, USA), grinding and dimpling (Dimple Grinder, Gatan Inc., Pennsylvania, USA) and Ar^+ ion-milling (Pips 691, Gatan Inc., California, USA) at an angle of 10° until perforation for TEM observations.

2.2 Electron microscopy

Scanning electron microscopy (JSM-5800, Jeol Inc., Tokyo, Japan) was used to inspect the microstructures. Transmission electron microscopy (TEM) investigations of the samples were performed using a field-emission-gun TEM (JEM-2010F, Jeol Inc., Japan) with an ultra-high-resolution pole piece, operated at 200 kV. The microscope is equipped with a Si (Li) EDS detector fitted into an atmospheric thin-window EDS spectrometer (Link ISIS 300, Oxford Instruments, England) that was used to acquire series of EDS spectra for quantification of Sn content in the IB-layer. Experimental HRTEM images were recorded in thin crystal part near high-contrast conditions, *i.e.* Scherzer focus and first reverse passband to facilitate identification of atomic column positions. Image simulations were performed using multislice algorithm (EMS software [67]) employing electron-optical parameters of the

microscope: C_s = 0.48 mm, Δf = 8 nm and θ_c = 1.2 mrad. High resolution HAADF- and ABF-STEM images of IBs in SnO_2-doped ZnO were recorded using a dedicated probe corrected scanning transmission electron microscope (JEM-ARM200CF, Jeol Ltd., Tokyo, Japan) operated at 200 kV.

2.3 Structural modeling

For initial supercells, unit-cell parameters of ZnO were used according to Kisi & Elcombe [68]: a = 3.2501 Å, c = 5.2071 Å, u = 0.3817. Structural modeling was performed following the methodology described by Ribić *et al.* [69]. Briefly, the models were generated by CrystalMaker® software [70] in such a manner that IB-plane is placed at the center of the supercell at the middle of its longer A-axis running parallel with the polar c-axis of ZnO. IB stacking and polarity inversion disrupts the lattice periodicity along the supercell A-axis, whereas the structure is periodic along the B- and C-axes. The continuity of the supercells was handled by adding an 8-Å-thick vacuum layer between the adjacent supercells along the non-periodic A-axis and adequate numbers of H-atoms were added to super-cell terminations to preserve the overall charge neutrality. Two different cations ordering were contemplated into the models, following the well-known IB_3 stacking sequence for Sn-rich IBs [17].

2.4 DFT calculations

The methodology of *ab-initio* calculations adhered to the methodology described by Ribić *et al.* [69]. Structural relaxations were based on the density functional theory (DFT) as implemented in the Quantum-Espresso code [71]. The Perdew-Burke-Ernzerhof (PBE) generalized gradient approximation [72] is applied to exchange correlation functional. Atomic potentials are described by ultrasoft pseudopotentials, with the 3d electrons of Zn included in the valence shell. Single particle electronic wavefunctions are expanded into plane-waves up to a kinetic energy cut-off at 30 Ry. A regular (4×4×4) grid of k-points is used to sample the 3D Brillouin zone for the bulk and 1×2×1 for supercells. We used 0.02 Ry of the Gaussian spreading for Brillouin-zone integration and Marzari-Vanderbilt cold smearing.

3. Results and Discussion

3.1 General characteristics of the Sn-doped ZnO ceramics

Already with small additions of SnO_2 (0.1 mol%) IBs are observed in ZnO grains, indicating that rather than forming a solid solution, SnO_2 instantly triggers the formation of IBs when added to ZnO, as described by Daneu *et al.* (2000). Fig. 1a shows a typical microstructure, where every ZnO grain contains a planar defect intersecting the grain. The inversion nature of these defects is revealed by the orientation of triangular etch-pits, that are inverted across the IB plane. Bright-field TEM image and the corresponding electron diffraction pattern in Fig. 1b show that IBs lie in basal planes. No streaks normal to {000l} reflections can be seen in the diffraction patterns in either $[2\bar{1}\bar{1}0]$ or $[01\bar{1}0]$ view, that would reflect ordering in the IB plane, such as in Sb-doped ZnO [69]. This indicates that we either have no long-range ordering, or the distribution of Sn-atoms is random in the IB-plane.

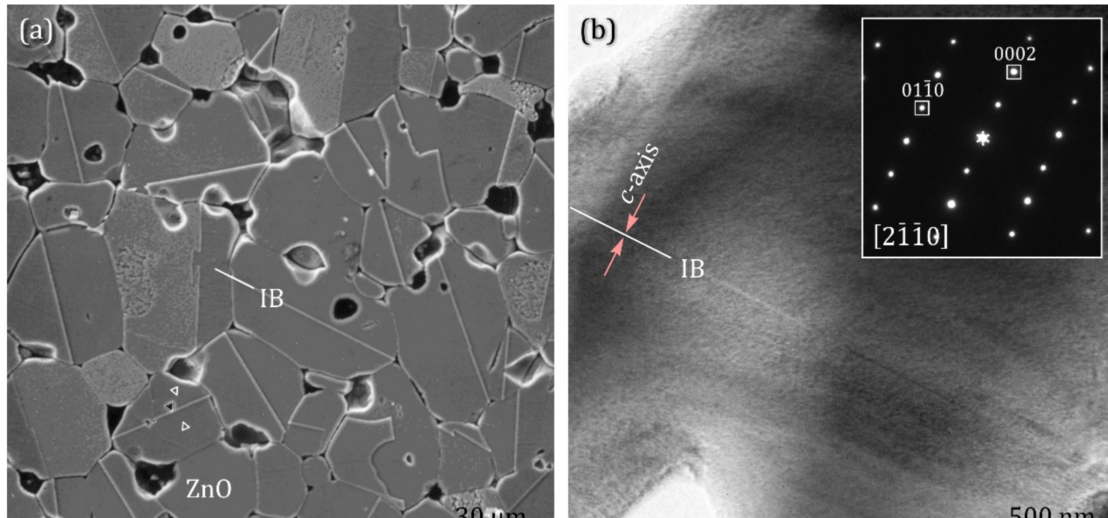

Fig. 1. Inversion boundaries (IB) in SnO_2-doped ZnO. (a) SEM image of ZnO–1mol% Bi_2O_3 ceramics doped by 0.1 mol% of SnO_2. After short etching of polished microstructure in dilute HCl the IBs appear as straight planar defects in ZnO grains. Triangular etch pits are pointing towards the IB-plane. Reproduced after Daneu *et al*. [7]. (b) BF-TEM image of IB in SnO_2-doped ZnO with a corresponding selected area electron diffraction pattern in $[2\bar{1}\bar{1}0]$ projection, indicating that IBs lie in basal planes of ZnO structure.

3.2 Local chemistry of the Sn-rich IBs

In order to solve the local structure of IBs an exact concentration of Sn in the IB-plane is the most essential information. The most suitable technique is EDS analysis of the boundary region. When detecting Sn in the IB plane some authors assumed a full monolayer of Sn [55, 56], while others suggested a partial occupation of IBs with Sn [59, 60, 63], and attempted to resolve this issue by different indirect techniques, such as measuring differences in the intensity profiles in STEM images [56, 59], that gave inconclusive results. Regardless these new attempts, the most reliable approach is still the one suggested by Walther et al. [16, 17], that relies on recording series of EDS spectra with series of different parallel beams, all centered at the single position on IB. Concentric electron probe (CEP) method, implementing EDS (or EELS), eliminates unwanted effects of variations in sample thickness largely improving the accuracy, while a high number of acquired spectra improves the precision [16]. Compared to the spatial difference method [73], CEP method provides 10^2-times better accuracy, and as much as 10-times improved precision [15-17], which is revolutionary for any quantitative analytical technique, especially the one measuring chemical compositions at atomic scale. Apart from quantitative determination of the dopant concentration, CEP method provides important information on the mode of dopant distribution in the area of interest, which is shown by the dependence of intensity ratio of traced elements (Sn and Zn) *vs.* beam radius. For example, if the dependence is asymptotic, approaching a finite intensity ratio, the dopant is present also in bulk material [74], however when the dependence is linear, the dopant stems only from the boundary [15].

The results of CEP/EDS method, implemented on Sn-rich IBs are shown in Fig. 2. Three CEP series, from small (limited by the boundary width) to large beam diameters (limited by the EDS detection limit of minor element), were measured on three different IBs. Linear dependence, as shown in Fig. 2, indicates that the Sn signal stems only from the IB plane, and that any Sn, if present in bulk ZnO, is below the detection limit. This suggests that

Sn is not present in solid solution, as proposed by some theoretical studies [75], but immediately forms an IB as soon as it enters the ZnO structure.

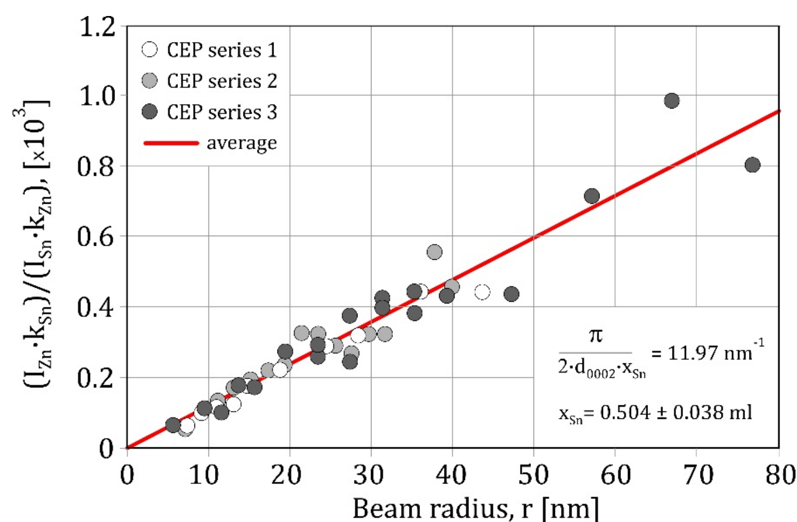

Fig. 2. The quantitative CEP/EDS analysis of the Sn-rich IBs in the ZnO wurtzite structure. Reproduced after Daneu *et al*. [17].

This result is a very important experimental evidence for the interpretation of physical properties, as bandgap, electron conductivity and optical transmittance [18-50]. Linear regression of measured data points, normalized with respect to thickness dependent threshold [15], gives a slope κ of 11.97 with a correlation coefficient R^2=0.9249. The slope is inversely proportional to the concentration of dopant, x_{Sn}, expressed in terms the apparent boundary width, w_{Sn}, that acquires its physical meaning when compared to a real lattice plane of the planar defect ($d_{IB} \approx c/2$), $w_{Sn} = x_{Sn} \cdot d_{IB}$, where the dopant concentration is measured [16]:

$$\frac{I_{Zn} \cdot k_{Sn}}{I_{Sn} \cdot k_{Zn}} = \kappa \cdot r + 1; \kappa = \frac{\pi}{2 \cdot w_{Sn}} \qquad (1)$$

with I_{Zn} and I_{Sn} corresponding to the intensities of measured elements, and k_{Zn} and k_{Sn} to their EDS k-factors, respectively. Hence, the apparent boundary width, w_{Sn} = 0.1312 ± 0.0099 nm. Assuming the width of one basal plane in ZnO structure [68] c/2 = 0.26035 nm, the fractional occupancy of cation sites, x_{Sn}, on the IB-plane is 0.504 ± 0.039, *i.e.* meaning that ½ of the IB layer is occupied by Sn^{4+} and the other ½ by Zn^{2+} atoms. This value exactly corresponds to the expected fractional occupancy for dopants with oxidation state of 4+, predicted by the charge balance model for IBs in ZnO [15]. In line with this model, shown in Fig. 3, charge balance on IB is distributed locally, following Pauling's rule of electroneutrality in ionic crystals. According to this principle, each O splits its charge equally to its neighbors. In ZnO structure, the ZnO_4 tetrahedra are linked by corners, which represent O-atoms. In each such corner 4 tetrahedra are connected, three from the same layer, and another from the adjacent layer. Each O-atom thus splits its charge to four Zn-atoms, receiving 4-times ½·e^-, that compensates its oxidation state of 2+. If now the same principle is applied to the octahedral IB layer, one can conclude that, each O-atom of MO_6 octahedra, also has only 4 neighbors, just the same as in the ZnO structure. This is because the O-sublattice is unchanged, only the cations occupy different interstices within the hexagonal close packed (*hcp*) lattice. Each cation in octahedral site thus receives 6-times ½·e^- as there are 6 oxygens bonded to each octahedral M-cation. Consequently, the average charge of M-cations is 3+. If we now turn to the IB plane, composed of close-packed layer of MO_6 octahedra, it can accommodate cations

of any oxidation state, as long as their average oxidation state is 3+. In the case of Sn^{4+}, this cation can thus occupy only ½ of the octahedral sites, while the rest is occupied by Zn^{2+} giving rise to complex 2D structures with an uncommon octahedral coordination of Zn.

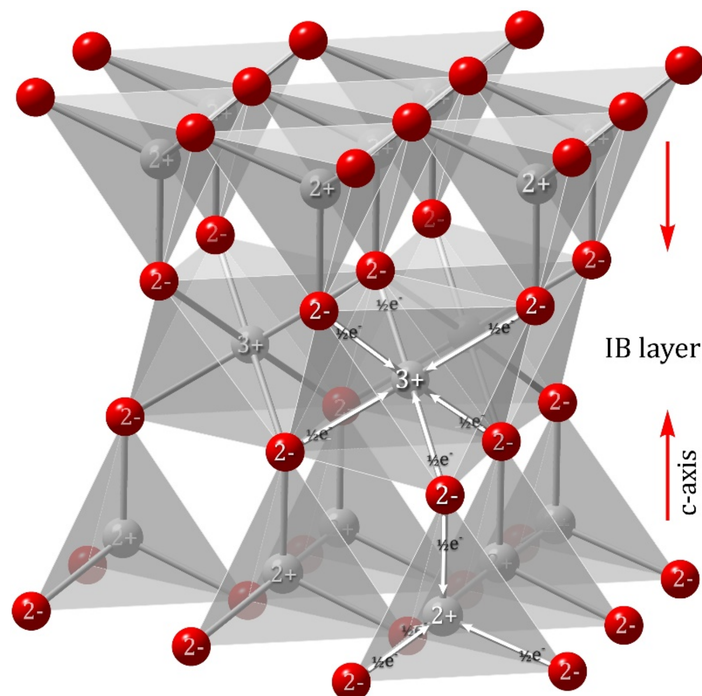

Fig. 3. Charge balance at the IB in ZnO according to Rečnik *et al.* [15]. White arrows indicate charge contributions from the O-atoms in tetrahedral and octahedral sites, yielding oxidation states of 2+ and 3+, respectively. The increase in the oxidation state in octahedral sites is due to the increased coordination number. The red arrows indicate the polar c-axis orientations across the IB-layer.

With time passed and a load of new publications in the field, the description of charge balance conditions on IBs [15] and accurate spectroscopic determination of the quantity of Sn in the IB layer [17], appear to have been lost. Without the use of proper analytical methodology and failing to study the previous work on Sn-rich IBs, Cao *et al.* [55] concluded that IBs in their $SnO_2(ZnO:Sn)_m$ nanowires are fully occupied by Sn. Similar conclusions were drawn a year later by Park *et al.* [56], followed by three further studies [57-59], where Tan *et al.* [59] nicely shows an intensity undulation in HAADF-STEM image indicating that the IB-layer is probably not fully occupied by Sn. On the other hand, it is great to read the studies by Eichhorn *et al.* [60] and Hoemke *et al.* [63] that have built on this knowledge and constructed fascinating modulated structures with parallel Sn-rich basal-plane IBs making use of either Ga_2O_3 or Al_2O_3 additions to stabilize the transient tail-to-tail configuration inbetween, respectively.

3.3 Translation of the Sn-rich IBs

To study the structure of IBs we inspected ZnO grains near $[2\bar{1}\bar{1}0]$ and $[01\bar{1}0]$ projections. Using HAADF-STEM imaging of the Sn-rich IBs it is rather straightforward to observe the increased intensity of the atomic columns constituting the IB plane, indicating the presence of heavy atoms. Fig. 4a shows a typical HAADF-STEM image of the Sn-rich IB in $[2\bar{1}\bar{1}0]$ projection with easily identifiable cation stacking across the IB plane. According to the recent classification of IBs by Ribić *et al.* [69], the cation stacking in the Sn-rich IB

corresponds to the lowest energy IB_3 translation, having the largest fraction of hexagonal bonds (*wow*). The stacking sequence corresponds to Aβ−Bα−AβC−γB−βC (with cation sites denoted by Greek, and anion sites by Latin letters) and is consistent with the observations of other authors [55-60, 63], suggesting that IB_3 is likely to be the only stable IB configuration in SnO_2-doped ZnO.

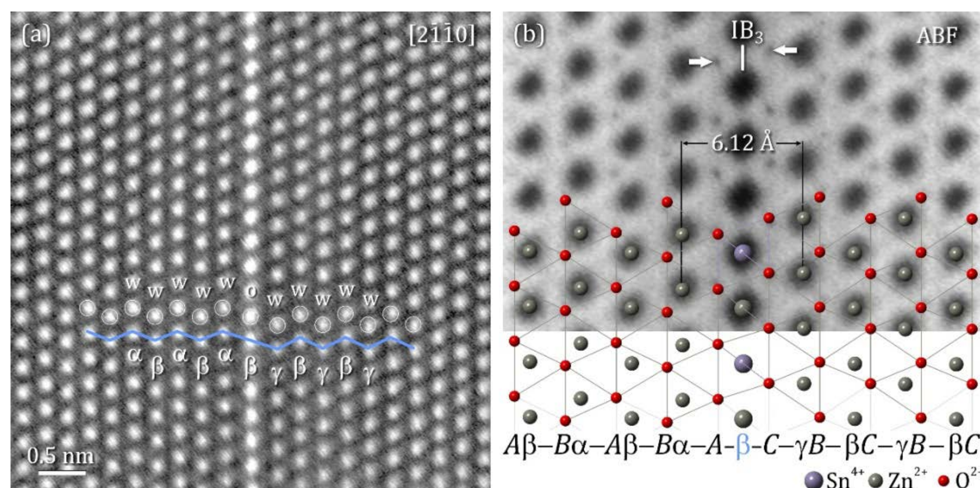

Fig. 4. High-resolution STEM images of the Sn-rich IB in [2$\bar{1}\bar{1}$0] projection. (a) HAADF-STEM image displaying a higher contrast for atomic columns along the IB-plane. Cation positions facilitate a direct identification of IB translation. (b) ABF-STEM image showing the positions of O-columns (weak dark dots). These assist us to identify the coordination of cations and the type of polarity inversion. Below is overlaid DFT relaxed model of the Sn-rich IB (s*tripes* variant of cation distribution) with a stacking sequence of IB_3 translation.

The ABF image of the Sn-rich IB in Fig. 4b, additionally reveals tiny dark dots that correspond to the positions of O-columns, that facilitate a straightforward identification of polarity inversion. Slanted triangles of weak dots enclosing large dark dots represent ZnO_4 tetrahedra in [2$\bar{1}\bar{1}$0] projection. These tetrahedra are pointing to the right in left domain, and to the left in right domain, confirming a head-to-head inversion. Even more interesting is the distribution of O-columns along the IB-plane. Here the cations move to central, flattened octahedral positions. Further we can observe that the size of octahedra varies along the IB-plane. This can be seen by a slight, but consistent alternating contraction/dilatation in O-positions at the focus plane of high-angular scanning. This variation is indicative of cations with a higher and lower oxidation states, imposing stronger or weaker attraction to the surrounding O-atoms, respectively. Measuring distances from STEM images is highly unreliable due to scanning distortions [76]. The simplest way to obtain some rough approximation of structural information is elimination of systematic distortions caused by sample drift during scanning. This can be done by geometrical correction of STEM image using real-space reference, which in our case is bulk ZnO. Once the images are corrected for systematic distortions, they can be used to measure the apparent expansion in the cation sublattice across the IB-plane (Zn–IB–Zn). The $d_{IB(Zn\text{-}Zn)}$ distance,[1] measured from several STEM images, normalized to bulk ZnO, amounts to 6.12 ± 0.10 Å. This value is slightly larger than the $d_{IB(Zn\text{-}Zn)}$ distance of the Sb-rich IB_3 reported by Ribić *et al.* [69] based on quantitative HRTEM (5.99 ± 0.05 Å), but we must keep in mind that the variations in the reported IB expansions measured from STEM images may be considerable. Park *et al.* [56] reported the $d_{IB(Zn\text{-}Zn)}$ distance of 6.02 Å for the SnO_2-doped ZnO nanobelts, which is similar

[1] Sublattice $\Delta_{IB(Zn\text{–}Zn)}$ expansion and $\Delta_{IB(O\text{-}O)}$ contraction are expressed in fractions of c -parameter of ZnO (c = 5.207 Å) through the following relations: $\Delta_{IB(Zn\text{–}Zn)} = [d_{IB(Zn\text{-}Zn)} - c]/c$ and $\Delta_{IB(O\text{-}O)} = \Delta_{IB(Zn\text{–}Zn)} + 0.5 - 2u$. *l.c.* Ref [68]

to that of the Sb-doped nanorods [77]. Other STEM images in their work vary from 5.55–6.45 Å, with their DFT optimized model predicting a $d_{IB(Zn\text{-}Zn)}$ distance of 6.35 Å. Jiang *et al.* [58] determined a similar value in the $SnO_2(ZnO:Sn)_m$ polytypoidic nanowires. The $d_{IB(Zn\text{-}Zn)}$ value reported by Eichhorn *et al.* [60] is considerably shorter, but we must keep in mind that these IBs are not directly comparable as they constitute a homologous $[Sn_{0.5}Zn_{0.5}]GaO_3(ZnO)_3$ phase. Shorter measured distances in homologous phases are probably due the presence of tail-to-tail inversion in vicinity that may influence head-to-head dilatation.

3.4 Cation distribution in the Sn-rich IBs

Visualizing cation distribution within the IB-layer is not an easy task. Ideally, we want to directly image the IB-plane along the [0001] axis of ZnO. The problem is that the IB-plane is buried within layers of ZnO, and there is no nondestructive way to remove them. Focused ion-beam (FIB) cutting of (0001) ZnO lamella with IB turns out to be unsuccessful because of deep damage, Ga^+ ion implantation, and the final TEM lamellae are too thick for structural work. Another approach is to search the conventional TEM sample for [0001] oriented ZnO grains and finding the IB in thin crystal foil. If IB does not exit exactly to the thin part of the crystal, the information on cation distribution is overshadowed by superimposed ZnO layers. Our HAADF-STEM and HRTEM image simulations demonstrate that already with more than 10-ZnO-layers (~2.6 nm thickness) on both sides of an IB-layer, no contrast features from IB can be observed. As there is no amplitude contrast produced by an in-plane IB to facilitate their identification at low magnifications, search for such cross-sections would need to be done in high-resolution mode, which is further complicated by rapid evaporation of ZnO due to electron irradiation. We therefore have to rely on conservative edge-on orientations, such as $[2\bar{1}\bar{1}0]$ and $[01\bar{1}0]$, and look forward to obtain all the information necessary to reconstruct 2D cation ordering in the IB plane from these projections [15].

When studying Sn-rich IBs at high resolution, we realize that all important contrast features are averaged out in crystal foils thicker than ~10 nm. This problem also appears to be the main obstacle in solving the cation distribution in Sn-rich IBs by other authors [55-59], where only the latest work shows some contrast variations along the IB-plane in $[01\bar{1}0]$ projection. Why this appears to be such a problem? Unlike in Sb-rich IBs, where we have pure Sb and Zn columns in any of $\langle 01\bar{1}0\rangle$ projections [15], in Sn-rich IBs, no atomic column remains pure at longer distances. Therefore, if we are to obtain any information on cation ordering, we must work in a thin crystal foil, and fast, because of the evaporation of ZnO, especially in scanning mode. Fig. 5 shows a HRTEM image of Sn-rich IB from a thin crystal part in $[01\bar{1}0]$ projection. The foil thickness in the area of Fig 5a is between 2-3 nm, calculated by $2d\cdot\tan\varphi$, where d is the distance from the crystal edge, and φ is the ion-milling angle.

Under these conditions, we observe interesting contrast variations along the IB-plane that give us a valuable hint on possible cation ordering. These contrast features are generated by two cation distributions that satisfy 1:1 ratio of Sn and Zn: (*i*) *zigzag* ordering with cations of the same species are forming chains of octahedra though the IB layer, and (*ii*) *stripe* with the cations of the same species occupying octahedra in linear manner, as illustrated in Fig. 6.

Because the crystal foil is very thin we have a fair chance to observe sequences of pure cation distributions. The two characteristic arrangements are outlined in Fig. 5a, and the corresponding simulated images are shown in Figs. 5b and 5c. Under chosen imaging conditions, near the first reverse passband of the contrast transfer function, bright dots in the image roughly correspond to the position of cation columns. In the first arrangement, strong and weaker bright dots are alternating along the interface, while the second arrangement is characterized by doublets of strong and weak dots. As seen by simulations, the intensity of bright dots along the IB-plane directly corresponds to the positions of Sn-columns, while the weaker dots inbetween correspond to the Zn-columns.

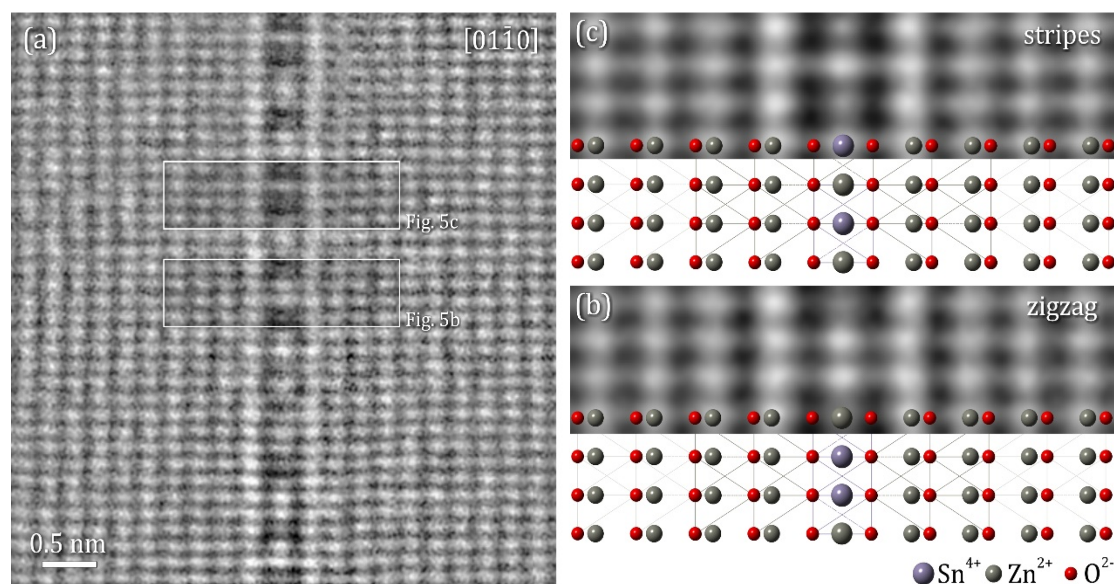

Fig. 5. The quantitative HRTEM study of the Sn-rich IB in [01$\bar{1}$0] projection. (a) High-resolution HRTEM image with the evident cation distribution along the IB-plane. Two typical sequences are observed (outlined). The simulated HRTEM images based on (b) *zigzag*, and (**c**) *stripes* cation ordering with overlaid structure models. Simulated images were calculated for 2.8 nm thick crystal and a focus value of -72 nm.

3.5 DFT study of cation ordering in the Sn-rich IBs

The 1:1 distribution of two atomic species is optimally accomplished in the square packing of atoms, *i.e.* chessboard arrangement. In a hexagonal close packing, such as that in the IB layer, monotonous distribution of two species in 1:1 ratio is not possible. To satisfy the charge balance requirements (Section 3.2) we must destroy the hexagonal in-plane symmetry of the octahedral IB layer. This instantly implies complex arrangements of the two cations. It can be shown that the simplest distributions are also the shortest-range, having the smallest periodic units. The *zigzag* ordering suggested by Daneu *et al.* [17] seems a good solution for short-range distribution of the two cations in the IB plane, however this alone is not sufficient to generate a maximum degree of freedom for cation ordering. Here we add *stripe* distribution, which has a half smaller repeat unit compared to *zigzag* ordering and helps increasing the entropy of the IB layer.

The two cationic arrangements, *zigzag* and *stripe*, are illustrated in Figs. 6a and 6b. Both distributions maintain Sn:Zn ratio at 1:1 at short range. These two arrangements have the shortest possible repeat units, with the *zigzag* containing four cations, and the *stripe* only two, which is the lowest possible minimum. Our DFT calculations show that *stripe* distribution has only slightly lower energy (6 meV/*f.u.*) than the *zigzag* distribution, which makes them thermodynamically very competitive. The energy difference arises mainly from larger variation in the bond lengths and angles in the *zigzag* model (Fig. 6c) compared to the more symmetric *stripe* model (Fig. 6d). Such small energy difference is easily overcome kinetically and both variants would be expected in real IB-layers.

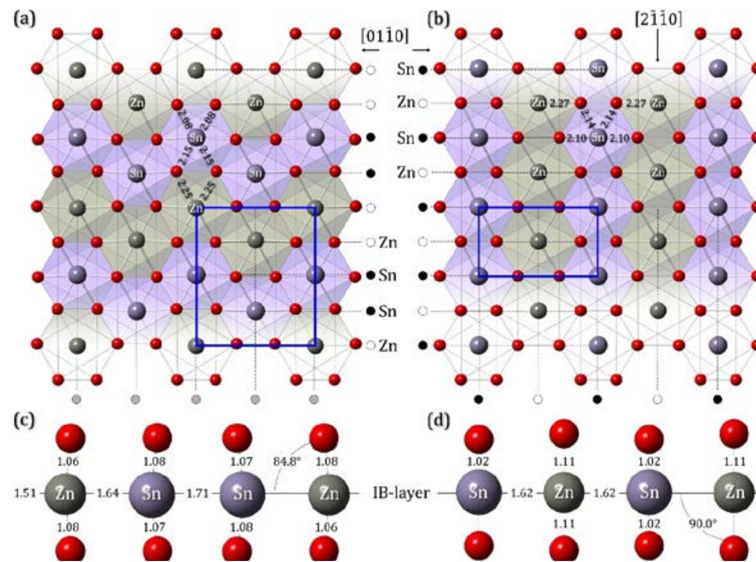

Fig. 6. Two possible short-range distributions of Sn and Zn in the Sn-rich IBs in ZnO. (a) *zigzag* distribution forming interwoven chains of octahedra. The repeat unit in this distribution contains two Sn and two Zn atoms. (b) *stripe* distribution forming linear arrays of octahedra with the repeat unit containing one Sn and one Zn atom. Bond lengths and angles in models, after DFT relaxation are shown in (c) for *zigzag* and (d) for *stripe* setting.

If we take a close look at the HRTEM image in Fig. 5a, we indeed see segments of both elementary distributions, as well as their combinations. As both configurations are energetically equivalent and the system tends to randomize Sn and Zn atoms as much as possible, the elementary segments are only stable at short lengths, barely enough that we observe them in a very thin crystal foil. As the crystal thickness increases, we see less and less clearly any of the two sequences, as the cation ordering changes the type and the direction, intermittently, at any moment, to maximize the layer entropy that is driven by local charge balance. This is the main reason why we do not observe ordering in diffraction patterns or high-resolution images of Sn-rich IBs in thick crystals.

While Sn-doped IB already acts as a quantum well for scattering of phonons [78], the long-range in-plane disorder, as a high entropy 2D object, additionally contributes to phonon dissipation. On the other hand, Zn^{2+} located in very uncommon octahedral sites, would modify the bandgap, and possibly also enhance the in-plane conductivity of carriers. Theoretical studies of IBs have recently shown a great potential in studying potential barriers in ZnO [79, 80]. To study the long-range ordering of cations in the Sn-rich IBs, molecular dynamic calculations on larger scale should be performed. This can be computationally demanding but knowing the exact in-plane structure can contribute to better understanding physical properties important for optoelectronic, thermoelectrics, varistors and other applications.

4. Conclusion

We investigated the head-to-head basal plane inversion boundaries in Sn doped ZnO wurtzite structure using HRTEM and STEM analysis and DFT calculations. Even small additions of SnO_2 (0.1 mol%) trigger the formation of IBs in ZnO grains, indicating the high preference of SnO_2 in forming planar defects rather than a solid solution with ZnO. Understanding the local structure of the Sn-rich IBs has been shown to be very important for

the interpretation of physical properties of Sn-doped ZnO materials, such as bandgap, electron conductivity and optical transmittance. Here we revised published data on structural properties in the Sn-doped ZnO IBs, and attempted to add the missing part, which refers to in-plane cation ordering in IB layer. To summarize important aspects of structural characterization discussed in this paper:

- The positions of O-columns shown by ABF-STEM confirm head-to-head inversion of the Sn-rich IBs in ZnO, and illustrates that cations in the IB-plane occupy octahedral interstices.
- As shown by quantitative CEP/EDS analysis, the Sn-rich IBs obey the stringent 3+ rule for the average oxidation state of octahedral cations comprising a basal-plane IB. Following this rule, one half of the IB-layer is occupied by Sn^{4+}, and the other half by Zn^{2+} cations.
- The translation state of the Sn-rich IBs corresponds to the $A\beta{-}B\alpha{-}A\beta C{-}\gamma B{-}\beta C$ (IB_3) sequence, and is consistent with the observations in the other studies, suggesting that this is likely the only stable IB configuration in SnO_2-doped ZnO.
- Based on the quantitative HRTEM and HAADF–STEM analysis of in-plane ordering of Sn and Zn atoms two types of short-range distributions were identified, *zigzag* and *stripe*. DFT calculations showed that both cation distributions are energetically equivalent and randomly alternate throughout the structure, what can be also observed on HRTEM images.

Acknowledgments

This study is based on part of the Ph.D. thesis of Vesna Ribić. The authors gratefully acknowledge the NSC cluster at IJS (Ljubljana) for the access and continuous support. We thank Tina Radošević from Nanostructured Materials Department for TEM samples preparation and Center for Electron Microscopy (CEM) from JSI for the access to the electron microscopy facilities. This work was supported by the Ministry of Education, Science and Technological Development of the Republic of Serbia (Grant No. 451-03-9/2021-14/200053), the Slovenian Research Agency (Program No. P2-0084, Project No. J1-9177), Slovenian-Serbian bilateral Projects (BI-RS/16-17-053 and BI-RS/18-19-026) and the European Union's Horizon 2020 research and innovation program under grant agreement No 823717 - ESTEEM3.

5. References

1. M. Matsuoka, Jpn. J. Appl. Phys. 10/6 (1971) 736−746. https://doi.org/10.1143/JJAP.10.736
2. O. Milošević, D. Vasović, D. Poleti, L. Karanović, V. Petrović, D. Uskoković, Progress in Preparation of ZnO Based Varistor Ceramics. In: D.P. Uskoković, H. Palmour, R.M. Spriggs (Eds) Science of Sintering. Springer, Boston, MA, 1989. https://doi.org/10.1007/978-1-4899-0933-6_8
3. M. Žunić, Z. Branković, G. Branković, Sci. Sinter. 38 (2006) 161–167. http://doi.org/10.2298/SOS0602161Z
4. Ö. Özer, E. Suvaci, S. Bernik, Acta Mater. 58/12 (2010) 4126–4136. https://doi.org/10.1016/j.actamat.2010.04.003
5. R. D. Gould, B. A. Carter, J. Phys. D: Appl. Phys. 16/10 (1983) L201–L206. https://doi.org/10.1088/0022-3727/16/10/004

6. O. Milošević, P. Kostić, V. Petrović and D. Uskoković, Sci. Sintering 15/3 (1983) 121–130.
7. N. Daneu, A. Rečnik, S. Bernik, D. Kolar, J. Am. Ceram. Soc. 83 (2000) 3165–3171. https://doi.org/10.1111/j.1151-2916.2000.tb01699.x
8. S. Bernik, N. Daneu, J. Eur.Ceram. Soc. 21/10 (2001) 1879–1882. https://doi.org/10.1016/S0955-2219(01)00135-2
9. N. Daneu, A. Rečnik, S. Bernik, J. Am. Ceram. Soc. 86/8 (2003) 1379–1384. https://doi.org/10.1111/j.1151-2916.2003.tb03479.x
10. A. Rečnik, N. Daneu, S. Bernik, J. Eur. Ceram. Soc. 27 (2007) 1999–2008. https://doi.org/10.1016/j.jeurceramsoc.2006.06.006
11. N. Daneu, A. Rečnik, S. Bernik, J. Am. Ceram. Soc. 94/5 (2011) 1619–1626. https://doi.org/10.1111/j.1551-2916.2010.04290.x
12. A. Rečnik, S. Bernik, N. Daneu, J. Mater. Sci. 47 (2012), 1655–1668. https://doi.org/10.1007/s10853-011-5937-2
13. S. Bernik, J. Bernard, N. Daneu, A. Rečnik, J. Am. Ceram. Soc. 90/10 (2007) 3239–3247. https://doi.org/10.1111/j.1551-2916.2007.01886.x
14. T. Ivetić, M. V. Nikolić, M. Slankamenac, M. Živanov, D. Minić, P. M. Nikolić, M. M. Ristić, Sci. Sinter. 39 (2007) 229-240. https://doi.org/10.2298/SOS0703229I
15. A. Rečnik, N. Daneu, T. Walther, W. Mader, J. Am. Ceram. Soc. 84/11 (2001) 2657–2668. https://doi.org/10.1111/j.1151-2916.2001.tb01068.x
16. T. Walther, N. Daneu, A. Rečnik, Interface Sci. 12 (2004) 267–275. https://doi.org/10.1023/B:INTS.0000028656.12913.8a
17. . Daneu, A. Rečnik, T. Walther, W. Mader, Microsc. Microanal, 9 (2003) 286–287 https://doi.org/10.1017/S1431927603024024
18. S. Ilican, M. Caglar, Y. Caglar, Appl. Surf. Sci. 256 (2010) 7204–7210. https://doi.org/10.1016/j.apsusc.2010.05.052
19. M. Ajili, M. Castagné, N. K. Turki, Superlattices Microst. 53 (2013) 213–222. http://dx.doi.org/10.1016/j.spmi.2012.10.012
20. M. Vishwas, K. Narasimha Rao, K.V. Arjuna Gowda, R.P.S. Chakradhar, Spectrochim. Acta A: Molecular and Biomolecular Spectroscopy 95 (2012) 423–426. http://dx.doi.org/10.1016/j.saa.2012.04.006
21. S. Ishak, S. Johari, M. M. Ramli, AIP Conference Proceedings 2203 (2020) 020027. https://doi.org/10.1063/1.5142119
22. X. Li, Y. Chang, Y. Long, Mater. Sci. Eng. C 32 (2012) 817–821. https://doi.org/10.1016/j.msec.2012.01.032
23. S. C. Navale, I. S. Mulla, Mater. Sci. Eng. C 29 (2009) 1317–1320. https://doi.org/10.1016/j.msec.2008.09.050
24. S. T. Shishiyanu, T. S. Shishiyanu, O. I. Lupan, Sens. Actuators B Chem. 107 (2005) 379–386. https://doi.org/10.1016/j.snb.2004.10.030
25. S. Johnson Jeyakumar, J. Vasudevan, B. Arunkumar, M. Jothibas, A. Rajeswari, R. Sathiskumar, A. Muthuvel, Mater. Today: Proceedings 2020. in press. https://doi.org/10.1016/j.matpr.2020.09.376
26. M. S. Haseman, P. Saadatkia, J. T. Warfield, J. Lawrence, A. Hernandez, G. E. Jellison, L. A. Boatner, F. A. Selim, Journal of Elec Materi 47 (2018) 1497–1504. https://doi.org/10.1007/s11664-017-5942-6
27. V. Ganesh, I. S. Yahia, S. Al Faify, M. Shkir, J. Phys. Chem. Solids 100 (2017) 115–125. http://dx.doi.org/10.1016/j.jpcs.2016.09.022
28. F. Z. Bedia, A. Bedia, N. Maloufi, M. Aillerie, F. Genty, B. Benyouce, J. Alloys Compd. 616 (2014) 312–318. http://dx.doi.org/10.1016/j.jallcom.2014.07.086
29. Q. Humayun, M. Kashif, U. Hashim, J. Nanomater, 2013 (2013) ID792930–8. http://dx.doi.org/10.1155/2013/792930

30. C. Zegadi, K. Abdelkebir, D. Chaumont, M. Adnane, S. Hamzaoui, AMPC 4/5 (2014) 93–104. http://dx.doi.org/10.4236/ampc.2014.45012
31. A. D. Acharya, S. Moghe, R. Panda, S. B. Shrivastava, M. Gangrade, T. Shripathi, D.M. Phase, V. Ganesan, J. Mol. Struct. 1022 (2012) 8–15. https://doi.org/10.1016/j.molstruc.2012.04.044
32. W. E. Mahmoud, T. Al-Harbi, J. Cryst. Growth 327/1 (2011) 52–56. https://doi.org/10.1016/j.jcrysgro.2011.05.003
33. Y. Andolsi, F. Chaabouni, M. Abaab, J Mater Sci: Mater Electron 28 (2017) 8347–8358. https://doi.org/10.1007/s10854-017-6551-0
34. M. Zaharescu, S. Mihaiu, A. Toader, I. Atkinson, J. Calderon-Moreno, M. Anastasescu, M. Nicolescu, M. Duta, M. Gartner, K. Vojisavljevic, B. Malic, V.A. Ivanov, E.P. Zaretskaya, Thin Solid Films 571/ 3 (2014) 727–734. https://doi.org/10.1016/j.tsf.2014.02.090
35. K. J. Chen, F. Y. Hung, Y. T. Chen, S. J. Chang, Z. S. Hu, Mater. Trans. 51/ 7 (2010) 1340-1345. https://doi.org/10.2320/matertrans.M2009378
36. C-J. Huang, M-C. Chiu, H-C. Yao, D-C. Tsai, F-S. Shieu, J. Electrochem. Soc. 155/12 (2008) K211-K218. https://doi.org/10.1149/1.2992082
37. M. R. Vaezi, S. K. Sadrnezhaad, Mater. Sci. Eng. B 141 (2007) 23–27. https://doi.org/10.1016/j.mseb.2007.05.010
38. A. Bougrine, M. Addoua, A. Kachouane, J.C. Bérnède, M. Morsli, Mater. Chem. Phys. 91/2 (2005) 247–252. https://doi.org/10.1016/j.matchemphys.2003.11.033
39. E. López ‐ Ponce, J. L. Costa ‐ Krämer, M. S. Martín ‐ González, F. Briones, J. F. Fernández, A. C. Caballero, M. Villegas, J. de Frutos, Phys. Stat. Sol. 203/6 (2006) 1383–1389. https://doi.org/10.1002/pssa.200566177
40. I. Saurdi, M. H. Mamat, M. F. Malek, M. Rusop, Adv. Mater. Sci. Eng. 2014 (2014) ID 636725–8. http://dx.doi.org/10.1155/2014/636725
41. H. Wang, R. Bhattacharjee, I-M. Hung, L. Li, R. Zeng, Electroch. Acta 111 (2013) 797– 801. http://dx.doi.org/10.1016/j.electacta.2013.07.199
42. S. Ameen, M. S. Akhtar, H-K. Seo, Y. S. Kim, H. S. Shin, Chemical. Eng. J. 187 (2012) 351–356. https://doi.org/10.1016/j.cej.2012.01.097
43. N. Ye, J. Qi, Z. Qi, X. Zhang, Y. Yang, J. Liu, Y. Zhang, J. Power Sources 195 (2010) 5806–5809. https://doi.org/10.1016/j.jpowsour.2010.03.036
44. K. G. Kumar, P. B. Bhargav, N. Ahmed, C. Balaji, Trans. Electr. Electron. Mater. (2021). https://doi.org/10.1007/s42341-021-00301-8
45. N. Venkatesh, S. Aravindan, K. Ramki, G. Murugadoss, R. Thangamuthu, P. Sakthivel, Environ. Sci. Pollut. Res. 28 (2021) 16792–16803. https://doi.org/10.1007/s11356-020-11763-3
46. J-H. Sun, S-Y. Dong, J-L. Feng, X-J. Yin, X-C. Zhao, J. Mol. Catal. A Chem. 335/1 (2011) 145–150. https://doi.org/10.1016/j.molcata.2010.11.026
47. M. Manikandan, P. Rajagopalan, N. Patra, S. Jayachandran, M. Muralidharan, S. S. Mani Prabu, I. A. Palani, V. Singh, Nanotechnology 31/13 (2020) 185401. https://doi.org/10.1088/1361-6528/ab6b9e
48. D. V. Vu, D. H. Le, T. T. Nguyen, T. V. Duong, Q. D. Ngo, T. Q. Trinh, J. Mater. Sci.: Mater. Electron. 30 (2019) 6544–6551. https://doi.org/10.1007/s10854-019-00960-7
49. M. Verma, P. K. Dwivedi, B. Das, J. Exp. Nanosci. 10/6 (2015) 438–448. https://doi.org/10.1080/17458080.2013.840936
50. S. Y. Li, P. Lin, C. Y. Lee, T. Y. Tseng, C. J. Huang, J. Phys. D: Appl. Phys. 37 (2004) 2274–2282. https://doi.org/10.1088/0022-3727/37/16/009
51. I. Cora, Zs. Fogarassy, R. Fornari, M. Bosi, A. Rečnik, B. Pécz, Acta Mater. 183 (2020) 216–227. https://doi.org/10.1016/j.actamat.2019.11.019

52. R. Deng, X. Zhang, E. Zhang, Y. Liang, Z. Liu, H. Xu, S. Hark, J. Phys. Chem. C 111 (2007) 13013–13015. https://doi.org/10.1021/jp073668
53. N. Zhang, R. C. Che, J. Shen, W. Y. Zhou, X. F. Duan, Appl Phys A 97 (2009) 943–946. https://doi.org/10.1007/s00339-009-5367-z
54. R. Yousefi, CrystEngComm 17 (2015) 2698–2704. https://doi.org/10.1039/c5ce00316d
55. B. Cao, T. Shi, S. Zheng, Y. H. Ikuhara, W. Zhou, D. Wood, M. Al-Jassim, Y. Yan, J. Phys. Chem. C 116 (2012) 5009−5013. https://doi.org/10.1021/jp211135r
56. Y. C. Park, Y. H. Kim, H. Nahm, J. Noh, Y. Kim, J. Kim, W. Lee, J. Yang, J. Park, Appl. Phys. Lett. 102 (2013) 033103–5. http://dx.doi.org/10.1063/1.4788812
57. S. Kim, S. Na, H. Jeon, S. Kim, B. Lee, J. Yang, H. Kim, H. J. Lee, Nanotechnology 24 (2013) 065703–065709. https://doi.org/10.1088/0957-4484/24/6/065703
58. S. Jiang, B. Ge, B. Xu, Q. Wang, B. Cao, CrystEngComm 20 (2018) 556–562. https://doi.org/10.1039/c7ce02014g
59. Tan 2020. Aluminium, CrystEngComm 22 (2020) 5355–5362. https://doi.org/10.1039/d0ce00889c
60. S. Eichhorn, H. Schmid, W. Assenmacher, W. Mader, J. Solid State Chem. 246 (2017) 214–220. http://doi.org/10.1016/j.jssc.2016.11.031
61. A. Goldstein, S. Andrews, R. Berger, V. Radmilović, J. Neaton, P. Yang, ACS Nano 7/12 (2013) 10747−10751. https://doi.org/10.1021/nn403836d
62. M. Bitenc, G. Dražić, Z. Crnjak Orel, Cryst. Growth Des. 10 (2010) 830–837. https://doi.org/10.1021/cg901193g
63. J. Hoemke, E. Tochigi, T. Tohei, H. Yoshida, N. Shibata, Y. Ikuhara, Y. Sakka, J. Am. Ceram. Soc. 101 (2018) 2616–2626. http://doi.org/10.1111/jace.15426
64. H. Schmid, E. Okunishi, W. Mader, Ultramicroscopy 127 (2013), 76–84. https://doi.org/10.1016/j.ultramic.2012.07.014
65. N. Daneu, N. Novak Gramc, A. Rečnik, M. Maček Kržmanc, S. Bernik, J. Eur. Ceram. Soc. 33 (2013) 335–344. https://doi.org/10.1016/j.jeurceramsoc.2012.08.023
66. A. Dapčević, A. Radojković, M. Žunić, M. Počuča-Nešić, O. Milošević, G. Branković, Sci. Sinter. 53 (2021) 55–66. https://doi.org/10.2298/SOS2101055D
67. P.A. Stadelmann, Ultramicroscopy 21/2 (1987) 131–145. https://doi.org/10.1016/0304-3991(87)90080-5
68. E. H. Kisi, M. M. Elcombe, Acta Cryst. C 45 (1989) 1867–1870. https://doi.org/10.1107/S0108270189004269
69. V. Ribić, A. Rečnik, M. Komelj, A. Kokalj, Z. Branković, M. Zlatović, G. Branković, Acta Mater. 199 (2020) 633–648. https://doi.org/10.1016/j.actamat.2020.08.035
70. D. C. Palmer, CrystalMaker software, Z. Kristallogr. 230/9 ‐ 10 (2015) 559–572. https://doi.org/10.1515/zkri-2015-1869
71. Giannozzi, S. Baroni, N. Bonini, M. Calandra, R. Car, C. Cavazzoni, D. Ceresoli, G. L. Chiarotti, M. Cococcioni, I. Dabo, A. D. Corso, S. de Gironcoli, S. Fabris, G. Fratesi, R. Gebauer, U. Gerstmann, C. Gougoussis, A. Kokalj, M. Lazzeri, L. Martin ‐ Samos, N. Marzari, F. Mauri, R. Mazzarello, S. Paolini, A. Pasquarello, L. Paulatto, C. Sbraccia, S. Scandolo, G. Sclauzero, A. P Seitsonen, A. Smogunov, P. Umari, R. M Wentzcovitch, J. Phys.: Condens. Matter 21/39 (2009) 395502–19, https://doi.org/10.1088/0953-8984/21/39/395502
72. J. P. Perdew, K. Burke, M. Ernzerhof, Phys Rev Lett. 77 (1996) 3865–3868. https://doi.org/10.1103/PhysRevLett.77.3865
73. J. Bruley, U. Bremer, V. Kraševec, J. Am. Ceram. Soc. 75/11 (1992)3127–3128. https://doi.org/10.1111/j.1151-2916.1992.tb04397.x
74. V. Šrot, A. Rečnik, C. Scheu, S. Šturm, B. Mirtič, Am. Mineral. 88 (2003) 1809–1816. https://doi.org/10.2138/am-2003-11-1222

75. Z. Xiong, L. Chen, C. He, Z. Liang, J. Phys.: Conf. Ser. 276 (2011) 012194–7. https://doi.org/10.1088/1742-6596/276/1/012194
76. A. Rečnik, G. Mobus, S. Šturm, Ultramicroscopy 103 (2005) 285–301. https://doi.org/10.1016/j.ultramic.2005.01.003
77. A.B. Yankovich, B. Puchala, F. Wang, J‐H. Seo, D. Morgan, X. Wang, Z. Ma, A. V. Kvit, P. M. Voyles, Nano Lett. 12 (2012) 1311−1316. https://doi.org/10.1021/nl203848t
78. S. Walia, S. Balendhran, H. Nili, S. Zhuiykov, G. Rosengarten, Q.H. Wang, M. Bhaskaran, S. Sriram, M.S. Strano, K. Kalantar-Zadeh, Progress in Materials Science 58 (2013) 1443–1489. https://doi.org/10.1016/j.pmatsci.2013.06.003
79. P. Keil, M. Trapp, N. Novak, T. Frömling, H.-J. Kleebe, and J. Rödel, Adv. Mater. 30 (2018) 1705573–11. https://doi.org/10.1111/jace.16912
80. J. Rohrer, K. Albe, Phys. Rev. Mater 5 (2021) 023601–11 https://doi.org/10.1103/PhysRevMaterials.5.023601

Сажетак: *У нашем недавном раду (Ribić et al. 2020) разматрали смо структуру инверзних граница (ИГ) у Sb_2O_3 допираном ZnO, док се у овом фокусирамо на ИГ које настају у SnO_2 допираном ZnO. Коришћењем метода скенирајуће трансмисионе електронске микроскопије са атомском резолуцијом (STEM) потврђујемо да се у SnO_2 допираном ZnO ИГ формирају у конфигурацији глава-глава, у којој су ZnO_4 тетраедри оба ZnO домена усмерени ка ИГ, састављеној од октаедраски координисаних атома Zn и Sn. Однос катјона у равни ИГ је дефинисан локалном равнотежом наелектрисања, која произилази из Паулинговог принципа електронеутралности за јонске кристале, према којем је просечно оксидационо стање катјона у равни ИГ 3+. Овај услов је испуњен кад је однос катјона у ИГ-слоју Sn^{4+} : Zn^{2+} = 1:1. Тај однос катјона утврђен је са енергетско-дисперзионом спектроскопијом (EDS) помоћу методе концентричних електронских снопова, која показује да атоми Sn заузимају 0,504 ± 0,039 слоја ИГ, док остатак октаедарских места заузима Zn. ИГ у SnO_2 допираном ZnO се јављају у транслационом стању $ИГ_3$ које поседује најнижу енергију. На Sn-допираној ИГ такође је прецизно утврђена експанзија катјонске подрешетке $ΔИГ_{(Zn-Zn)}$ од +91 pm са одговарајућом контракцијом О-подрешетке $ΔИГ_{(O-O)}$ од –46 pm. На основу квантитативне HRTEM анализе уређења атома Sn и Zn у ИГ равни, утврдили смо два могућа распореда катјона кратког домета, (а) цик-цак и (б) линијски. Наши прорачуни базирани на теорији функционала густине (DFT) показали су да је енергетска разлика између два распореда мала (~ 6 meV), што доводи до њиховог смењивања унутар октаедарског ИГ слоја. Као резултат, распоред катјона се наизменично мења, тежећи ка томе да се повећа унутрашња ентропија ИГ слоја, диригована локалном равнотежом наелектрисања и хексагоналним распоредом атома у ИГ равни. Одсуство дугодометне катјонске уређености промовише додатно расипање фонона на квантној јами, док би октаедарски координисан Zn^{2+} довео до промене енергетског процепа и повећао број носилаца наелектрисања у ИГ слоју.*
Кључне речи*: Инверзне доменске границе, SnO_2 допиран ZnO, инжењеринг поларности, термоелектрици, оптоелектроника.*

© 2021 Authors. Published by association for ETRAN Society. This article is an open access article distributed under the terms and conditions of the Creative Commons — Attribution 4.0 International license (https://creativecommons.org/licenses/by/4.0/).